Observation of a transition in the dynamics of strong-field atomic excitation

SongPo Xu,[1,2,*] MingQing Liu,[3,4,*] ShiLin Hu,[5] Zheng Shu,[3,4] Wei Quan ⓘ,[1,2,†] ZhiLei Xiao,[1,2] Yu Zhou,[1,2] MingZheng Wei,[1] Meng Zhao,[1,2] RenPing Sun,[1] YanLan Wang,[1,2] LinQiang Hua,[1,2] Cheng Gong,[1,2] XuanYang Lai,[1,2] Jing Chen,[3,6,‡] and XiaoJun Liu[1,2,§]

[1]*State Key Laboratory of Magnetic Resonance and Atomic and Molecular Physics, Wuhan Institute of Physics and Mathematics, Innovation Academy for Precision Measurement Science and Technology, Chinese Academy of Sciences, Wuhan 430071, China*
[2]*University of Chinese Academy of Sciences, Beijing 100049, China*
[3]*Institute of Applied Physics and Computational Mathematics, P. O. Box 8009, Beijing 100088, China*
[4]*HEDPS, Center for Applied Physics and Technology, Peking University, Beijing 100084, China*
[5]*Guangdong Provincial Key Laboratory of Quantum Metrology and Sensing, School of Physics and Astronomy, Sun Yat-Sen University (Zhuhai Campus), Zhuhai 519082, China*
[6]*Center for Advanced Material Diagnostic Technology, College of Engineering Physics, Shenzhen Technology University, Shenzhen 518118, China*

The consensus on the mechanism of atomic excitation in an intense laser field has not been reached so far because the proposed mechanisms may dominate in different regimes. In this paper, we show a clear transition of the underlying physical mechanism of strong-field atomic excitation from multiphoton resonance to coherent recapture by investigating the intensity dependence of the yields of neutral excited atoms (Ar*) and singly charged ions (Ar$^+$) of argon experimentally and theoretically. Our results indicate that, for 400 nm, the multiphoton resonance mechanism plays a significant role at low intensity and coherent recapture mechanism becomes important at high intensity. While for 800 nm, distinctive out-of-phase oscillations of Ar* and Ar$^+$ yields are identified, implying that coherent recapture mechanism dominates. Our work provides a more comprehensive understanding of the atomic excitation mechanism in an intense laser field.

I. INTRODUCTION

For atoms subject to an intense laser field, the ionization dynamics may be comprehended with either multiphoton ionization (MPI) or tunneling ionization (TI) [1–5]. To indicate the transition between these two limits, a pivotal role is given to the Keldysh parameter $\gamma = (I_p/2U_p)^{1/2}$ [6], where I_p is the atomic ionization potential and U_p the ponderomotive energy of the laser field. For $\gamma \gg 1$, MPI dominates and the ionization rate can be calculated by the perturbation theory. For $\gamma \ll 1$, TI becomes important and the features of photoelectron spectra can be largely understood by the classical dynamics. The validity of the Keldysh picture in describing the electron dynamics in strong laser field has been well verified experimentally in both single- and double-ionization processes by, e.g., investigating the evolution of relevant photoelectron spectra from MPI to TI regimes [7–10]. In the former regime, a multitude of resonance structures and distinct above-threshold ionization (ATI) peaks in the photoelectron spectra are identified [8–11], while for the latter, smooth spectra have been presented [12–14].

In contrast to the above-mentioned atomic ionization dynamics in strong laser field, atomic excitation dynamics has

not yet been well comprehended. In the 1990s, significant yields of Rydberg atoms have been observed experimentally for Kr and Xe [15,16], which is ascribed to the resonances with ac-Stark-shifted Rydberg states. Additional experimental investigations (see, e.g., [17–19]) show that, for noble-gas atoms subject to strong laser fields, the structures on the curves of singly charged ion yields versus laser intensity can be attributed to the electron trapping in atomic excited states. The mechanism of interference stabilization [20,21] associated with the repopulation of the Rydberg states through Raman transitions has been employed to analyze and comprehend the experimental data.

On the other hand, in a recent experimental work [22], the measured neutral atoms of helium surviving the laser pulse in excited states and the rapid decrease of the excitation probability with the increase of laser ellipticity are comprehended with the proposed frustrated tunneling ionization (FTI) mechanism. Note that a similar recapture picture has also been proposed in a theoretical work by Wang *et al.* [23]. Further experimental evidences supporting the FTI (or recapture) mechanism have been documented recently [24–26]. Moreover, this mechanism has also been employed to comprehend the presence of atoms in very high-lying Rydberg states with principal quantum number $n \sim 120$ [27] and coherent extreme-ultraviolet emission from atoms exposed to a strong laser field [28].

Very recently, Rydberg state excitation (RSE) in an intense laser field has also been studied using numerical solution

---

*These authors contributed equally to this work.
†charlywing@wipm.ac.cn
‡chen_jing@iapcm.ac.cn
§xjliu@wipm.ac.cn

of time-dependent Schrödinger equation (TDSE) [29,30]. Li *et al.* demonstrate that the presence of excited states in intense laser field can be understood as continuation of ATI to negative energies in the Rydberg quasicontinuum and their stabilization due to the large orbital angular momenta [29]. Furthermore, it is predicted that the yields of both excitation and ionization display strong modulations that are out of phase in relation to each other as a consequence of channel closing in multiphoton processes. Note that this phenomenon has not been verified experimentally yet. On the other hand, Piraux *et al.* show that the features of ionization and excitation are compatible with the multiphoton excitation picture at 800 nm, where the ionization dynamics is in the nonadiabatic regime [30].

As one can tell from the above discussions, consensus on the mechanism of strong-field excitation has not been achieved yet. More importantly, the formation of a complete picture of this strong-field phenomenon is still hindered by the limited experimental works and, especially, the rather coarse measurement precision so far.

In this paper, we report the investigation of the atomic excitation dynamics and unveil a distinct transition of the underlying mechanisms from multiphoton resonance to coherent recapture. Our observation relies on simultaneously measuring and comparing the intensity dependence of the yields of ions Ar^+ and excited neutral atoms Ar^* at 400 and 800 nm. Note that, to perform reliable intensity-dependent measurements of the ion and neutral atom yields, it is of importance to keep the laser intensity uncertainty as low as possible. In our measurements, several special experimental efforts have been taken to eliminate at utmost the intensity uncertainties, which are usually induced by the laser power fluctuation and notorious focusing averaging effect. With these experimental efforts as discussed below in the experimental section, several interesting experimental findings are observed. At 400 nm, the yields of Ar^* show two remarkable increasing steps. The first step is accompanied by the increase of Ar^+ yields, while the second step is weaker and a local maximum of the Ar^* yields comes out at the intensity where the local minimum of Ar^+ yields appears. At 800 nm, we observe that the yields of Ar^+ and Ar^* exhibit a series of out-of-phase oscillations with the increasing of laser intensity. With a dedicated quantum model based on a coherent recapture picture of the RSE in intense laser field, the experimental result of 800 nm and high intensity part of 400 nm can be well reproduced. While, the calculation results are inconsistent with the measurements in low-intensity regime for 400 nm. Our result implies that a transition of the underlying mechanism from multiphoton resonance to coherent recapture occurs when the laser parameter transits from MPI to TI regime.

II. EXPERIMENTAL METHOD

The experiments have been performed for Ar subject to an intense linearly polarized laser field with a homemade setup outlined in Fig. 1. The laser beam is generated from a commercial Ti:sapphire femtosecond laser system (Legend, Coherent Inc.) with a repetition rate of 1 kHz and a center wavelength of 800 nm. The laser beam at 400 nm is produced by frequency doubling of the fundamental beam with a beta
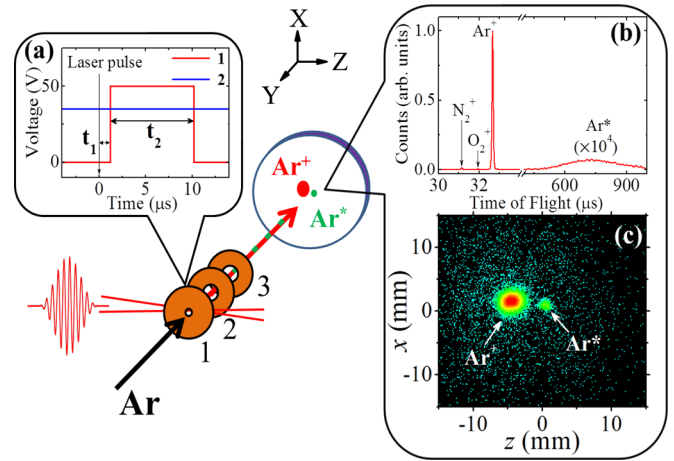

FIG. 1. Sketch of the experimental setup. A focused linearly polarized laser beam intersects a collimated supersonic beam of Ar in-between the electrode plates 1 and 2. The electric voltages are applied to the plates 1 and 2, as shown in (a), where $t_1 = 1.2 \, \mu$s and $t_2 = 9.0 \, \mu$s. Plate 3 is earthed. (b), (c) Show the typical time-of-flight spectrum and the image of Ar^+ and excited atoms Ar^* spatial distributions on the detector.

barium borate crystal. The laser pulse energy is precisely controlled with a combination of a broadband achromatic $\lambda/2$ plate and a thin-film polarizer. The pulse duration of the laser beam before entering the velocity map imaging (VMI) spectrometer is about 50 fs for both 400 and 800 nm. Before introduced into the spectrometer, the laser beam passes through an optical aperture with a diameter D of 4.0 (5.4) mm for 400 (800) nm to truncate the laser spot (with a diameter of 18 mm) near the focal lens.

The laser beam is directed into the vacuum chamber of a spectrometer, which is built based on the VMI technique [31]. In the interaction chamber of the spectrometer, the base pressure is maintained around 10^{-9} mbar. Inside this chamber, as shown in Fig. 1, there are three copper electrodes evenly spaced by 20 mm. Each electrode has a diameter of 90 mm and a thickness of 2 mm. The inner holes of electrodes 2 and 3 are 30 mm in diameter, while that of electrode 1 is 2 mm. A collimated supersonic atomic beam of Ar crosses with the laser beam at the spot midway between the centers of electrodes 1 and 2, and a pulsed and a constant electric field are applied to each of the electrodes, respectively. The pulsed (constant) electric voltages applied to electrode 1 (2) is 50 (35) V. The delay time (with respect to the laser pulse) and pulse width of the pulsed electric voltage (applied to electrode 1) are $t_1 = 1.2 \, \mu$s and $t_2 = 9.0 \, \mu$s. Electrode 3 is earthed during the experiments. Because the diameter of the supersonic beam is smaller than the Rayleigh length of the laser beam, the volume averaging effect can be suppressed significantly. Ar^+ and Ar^* produced by the laser field are detected by a position-sensitive microchannel plates (MCP) detector equipped with delay-line anode (DLD80 RoentDek Handels GmbH).

The geometry of the interaction volume has been determined carefully in our work. The beam waist w_0 can be determined by the formula $w_0 = \lambda f / D$ [32], where the focal lengths f of the convex lenses are 150 and 200 mm for
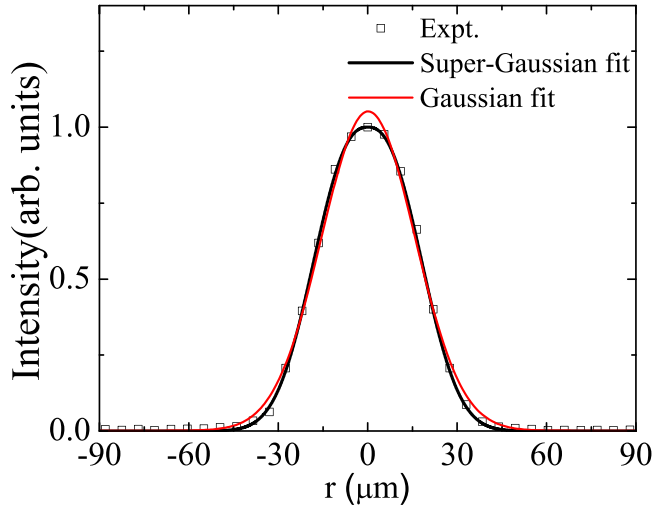
FIG. 2. The measured transverse spatial distribution of laser intensity at the laser focus ($z = 0$). The measurements have been fitted by a super-Gaussian function with $n = 2.45$ [see Eq. (B5)] and a Gaussian function, respectively.

wavelengths of 400 and 800 nm, respectively. The determined beam waists are 15.0 and 29.6 μm for the wavelengths of 400 and 800 nm, respectively. The laser intensity has been determined by the observed intensity dependence of the Freeman resonance peaks in photoelectron energy spectra [11]. With a commercial digital camera (WinCamD-LCM4, DataRay Inc.) with spatial resolution of 5.5 μm, we have measured the spatial distribution of laser intensity at the focus and, as shown in Fig. 2, it is found that the measured spatial distribution of intensity can be well fitted by a super-Gaussian (SG) function [33,34], instead of a Gaussian function. To determine the Rayleigh length, the yields of Ar$^+$ have been measured when the laser focus is moved along the propagation direction of the laser beam. The results are shown in Fig. 3. In the meantime,
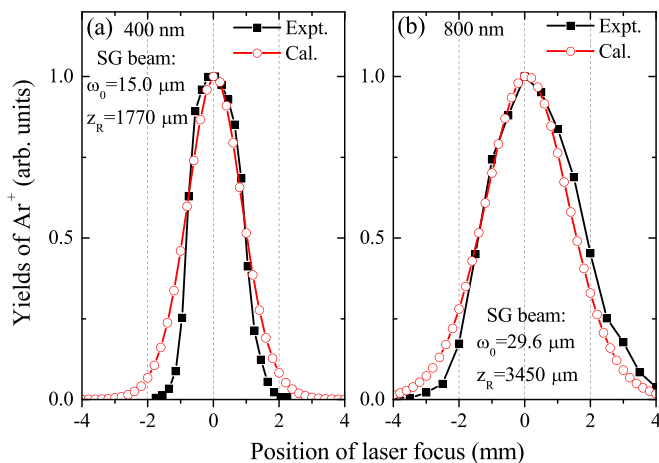

FIG. 3. The measured laser focus position dependence of the Ar$^+$ yields at (a) 400 nm and (b) 800 nm. The black solid squares indicate the measurements and the red open circles indicate the results calculated with a dedicated semiclassical model, where the spatial distributions of Gaussian laser beam and the spatial and velocity distributions of supersonic beam have been fully considered.

a semiclassical model has been applied to reproduce the measurements, as shown in Fig. 3, where the spatial distributions of the focused SG laser beam and the spatial and velocity distributions of supersonic beam [35] have been fully considered (for the details, see below). In this model, to achieve laser focus position dependence of the Ar$^+$ yields, the ionization rate of the single ionization event at each laser focus position is given by the Ammosov-Delone-Krainov (ADK) formula [36] and the Rayleigh length is the only free parameter left to be determined. With a careful comparison of calculations and measurements, the Rayleigh lengths in the laser beam focus are determined to be $z_R = 1770$ and 3450 μm for 400 and 800 nm, respectively. Note that an aperture with a radius of 250 μm is applied to collimate the supersonic beam. Considering that the radius of the aperture and also the geometry of the supersonic beam at the laser focus are much smaller than the Rayleigh length of the laser beam, the peak intensity along the laser propagation direction in the interaction area keeps almost constant. Hence, the influence of the volume averaging effect has been suppressed significantly in our work. This is important to consider the focal-volume averaging effect in the simulation, as will be shown below.

With our homemade specific spectrometer, advantages are obvious for investigation of excited atoms surviving the strong laser field. With the specific electric field scheme employed here, the light ions, e.g., H$^+$, H$_2$O$^+$, O$_2^+$, and N$_2^+$, etc., produced from the residual gases are pushed away and most of these ions cannot arrive at the detector. In contrast, heavy ions, e.g., Ar$^+$, and excited Ar atoms with quantum principal number $n \leqslant 75$ can be detected. This will significantly increase the signal-over-noise ratio for the detection of excited atoms, which is demonstrated in the typical time-of-flight (TOF) spectrum of Ar$^+$ and Ar*, as depicted in Fig. 1(b). On the other hand, the typical spatial distributions of Ar$^+$ and Ar* acquired by the detector are shown in Fig. 1(c), where the distribution of each particle can be well separated. Thus, by combining the TOF spectrum and the spatial distributions of Ar$^+$ and Ar*, we can extract the yields of each particle more precisely. During the data acquisition, the laser pulse energy is recorded shot by shot by a photodiode equipped with a homemade integration circuit. This circuit can transfer the measured energy signal to a delayed NIM pulse, which will be recorded by a computer along with the ionization and excitation yield signals for each laser pulse. To reduce the influence of the pulse-to-pulse intensity fluctuations on the measurements, in the off-line analysis, only the data with pulse energies in a small range are chosen to produce the spectra. In this way, the corresponding laser intensity fluctuation can be controlled to be around 2.0% and 0.6% for the data at 400 and 800 nm, respectively.

III. QUANTUM MODEL BASED ON STRONG-FIELD APPROXIMATION (SFA) THEORY

A quantum model based on the strong-field approximation (SFA) theory [6,37] of the RSE in intense laser field has been developed [38]. The advantage of this theoretical method over TDSE is that a clear physical picture behind RSE can be provided: first, the electron is pumped by the laser field into a continuum state from the ground state. Subsequently, it

evolves in the external field and, according to the calculation with our model, a small portion of the liberated electrons may be coherently captured into Rydberg states.

In our model [38], it is assumed that the electron is liberated by the laser field, propagates under its influence, and is captured into a Rydberg state at a later time. This is formalized by the transition amplitude (atomic units $m = \hbar = |e| = 1$ are used)

$$M_{nlm} = (-i)^2 \int_{-\infty}^{\infty} dt \int_{-\infty}^{t} dt' \int d^3\mathbf{k}$$
$$\times \langle \Phi_{nlm}^d(t) | V(\mathbf{r}) | \Phi_{\mathbf{k}}^{(V)}(t) \rangle \langle \Phi_{\mathbf{k}}^{(V)}(t') | \mathbf{r}' \cdot \mathbf{E}(t') | \Phi_i(t') \rangle, \quad (1)$$

where $|\Phi_i(t)\rangle$ is the initial ground state, $|\Phi_{\mathbf{k}}^{(V)}(t)\rangle$ the Volkov state with asymptotic momentum $\mathbf{k}$, and $|\Phi_{nlm}^d(t)\rangle$ the field-dressed Rydberg state with principal quantum number n, angular momentum quantum number l, and magnetic quantum number m (here $m = 0$ is assumed). $V(r) = -1/r$ is the binding potential and $\mathbf{E}(t) = E_0 \sin \omega t \hat{\mathbf{e}}_{\mathbf{z}}$ the 10-cycle laser electric field with the vector potential $\mathbf{A}(t) = E_0/\omega \cos \omega t \hat{\mathbf{e}}_{\mathbf{z}}$ ($\hat{\mathbf{e}}_{\mathbf{z}}$ is a unit polarization vector). The multiple integrals are performed by numerical integration with respect to t and t' and by saddle-point integration with respect to $\mathbf{k}$.

The wave function of the field-dressed Rydberg state can be approximately described as

$$\Phi_{nlm}^d(\mathbf{r}, t) = \phi_{nlm}(\mathbf{r}) e^{-iE_n t} e^{i\mathbf{r}\cdot\mathbf{A}(t)} e^{-i\int_{-\infty}^{t} d\tau A^2(\tau)/2}, \quad (2)$$

where $\phi_{nlm}(\mathbf{r})$ corresponds to a field-free Rydberg state with an energy $E_n = -1/(2n^2)$ and can be given by

$$\phi_{nlm}(\mathbf{r}) = N_{nl} R_{nl}(r) Y_{lm}(\theta, \varphi),$$
$$N_{nl} = \frac{(2\kappa_n)^{3/2}}{\Gamma(2l+2)} \sqrt{\frac{\Gamma(n+l+1)}{2n\Gamma(n-l)}},$$
$$R_{nl}(r) = (2\kappa_n r)^l e^{-\kappa_n r} {}_1F_1(-n+l+1, 2l+2, 2\kappa_n r), \quad (3)$$

where $\kappa_n = 1/n$, $Y_{lm}(\theta, \varphi)$ is a spherical harmonic function, and ${}_1F_1(x, y, z)$ the confluent hypergeometric function. More details of the derivations and calculations are given in Ref. [38].

IV. RESULTS AND DISCUSSIONS

In Fig. 4, the measured intensity dependence of the yields of Ar^+ and Ar^* at 400 [Fig. 4(a)] and 800 nm [Fig. 4(b)] are presented. At 400 nm, for Ar^+, a rapid rising trend in the low-intensity regime is clear. Meanwhile, a prominent sequence of steps can be identified in the intensity dependence of Ar^* yields. The first rapid enhancement in the intensity dependence of Ar^* yields appears around 190 TW/cm^2, which closely resembles the rising trend of Ar^+ yields. In fact, this enhancement has been also observed previously by Zimmermann *et al.* [39] and was ascribed to the closing of the six-photon ionization channel occurring at 190 TW/cm^2. Since channel closing occurs periodically at $n\hbar\omega = U_p + I_p$, where $\hbar\omega = 3.1$ eV is the photon energy and $I_p = 15.76$ eV the ionization energy of Ar atom, more steps are expected. Indeed, in our data, an additional second rapid enhancement in the intensity dependence of Ar^* yields comes out at
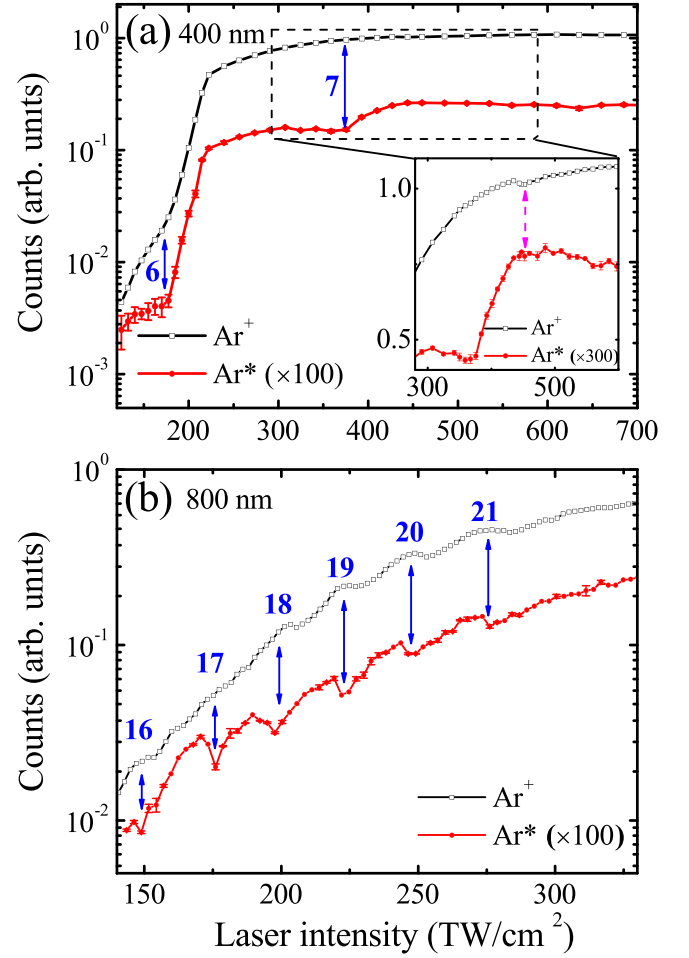

FIG. 4. The measured intensity dependence of the yields of ions Ar^+ and excited atoms Ar^*, which are multiplied by 100. The intensities, at which channel closings happen, are indicated by blue arrows. The laser wavelengthes are (a) 400 nm and (b) 800 nm. The data in the intensity interval of [280, 600 TW/cm^2] in (a) are zoomed out in the inset.

around 390 TW/cm^2, which can be ascribed to the closing of the seven-photon ionization channel. More interestingly, as shown by a magenta dashed arrow in the inset of Fig. 4(a), a clear local minimum of Ar^+ yields comes out at the intensity where the local maximum of Ar^* yields appears. Note that this feature is in stark contrast to that at 190 TW/cm^2, where synchronous increase of the Ar^+ and Ar^* yield is observed.

In Fig. 4(b), the measured intensity dependence of the yields of Ar^+ and Ar^* at 800 nm are shown. Similar to the appearance of local maximum of Ar^* yields and local minimum of Ar^+ yields at around 450 TW/cm^2 at 400 nm, both the Ar^+ and Ar^* yields exhibit pronounced oscillations with increasing laser intensity at 800 nm in Fig. 4(b), where the number of photons associated with the ionization channel closing are indicated with blue arrows at the corresponding intensities. The oscillation of Ar^* yields is out of phase in relation to that of Ar^+ yields, which is in accordance with the TDSE calculations [29,30].

Figure 5(a) presents the intensity dependence of total ionization (by SFA theory) and excitation yields calculated with
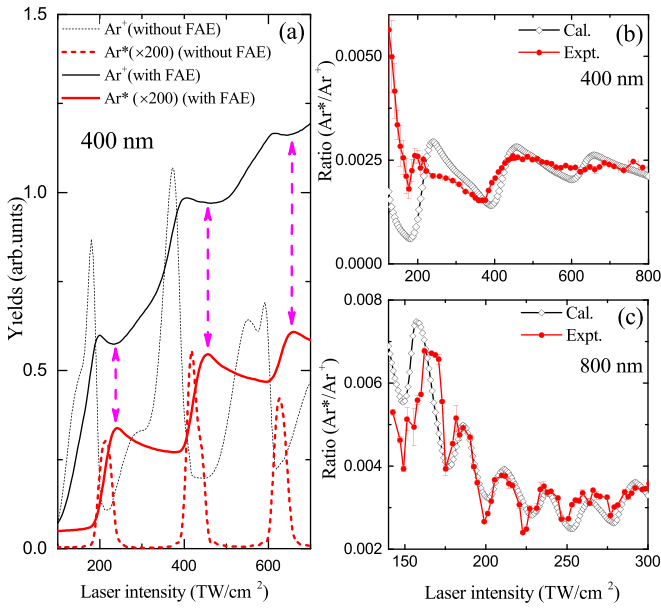
FIG. 5. (a) The calculated intensity dependence of ionization and excitation yields for Ar subject to a 400-nm laser field. Black lines: ionization yields calculated by length gauge SFA theory with and without focal averaging effect (FAE) included; red lines: intensity dependence of the RSE yields calculated by our quantum model with and without FAE included. The calculated excitation yield is a sum of the contributions of Rydberg states from $n = 5$ to 16 and has been multiplied by 200 for better visualization. (b) Ratio of excitation yield to ionization yield at 400 nm. (c) The same as (b) except that the wavelength of the laser field is 800 nm and the principal quantum number is in the range of $4 \leqslant n \leqslant 20$.

Eq. (1) for Ar subject to a 10-cycle laser field at 400 nm. The simulation results without focal averaging effect clearly show channel closing effect. At each channel closing intensity, the ionization yield becomes a minimum while the RSE probability increases very fast. This can be understood by the physical picture of our model [Eq. (1)]: The electron evolves in the external field after it is pumped into continuum; at the intensity with the channel closing condition fulfilled, part of the wave packet will be coherently captured into the Rydberg state and the other part of the wave packet goes to the detector as ATI, which results in out-of-phase oscillations in the intensity dependence of the ionization and RSE yields. With the focal averaging effect included, one finds that the peak structures in both ionization and RSE yields are smeared out to some extent. However, three steps corresponding to the peaks in RSE without focal averaging can be seen in the RSE probability and three local minima can be distinguished at intensities corresponding to the ends of the steps in the RSE (as indicated by vertical magenta dashed arrows). It is noteworthy that the step in the RSE and corresponding minimum in the ionization at about 450 TW/cm^2 are in good agreement with the experimental observations in Fig. 4(a) (and also in the inset). While, the ones around or above 600 TW/cm^2 cannot be seen in the experimental data which can be attributed to the saturation effect. Thus, with the good agreement between the measurements and calculations, it is revealed that the aforementioned coherent capture mechanism

plays a dominant role in the RSE in the high-intensity regime, i.e., from 300 to 500 TW/cm^2 at 400 nm.

To further explore the mechanism of RSE at 800 nm, in Fig. 5(c), the measured and calculated ratios of the RSE to ionization yields at 800 nm are presented. Both curves exhibit oscillations with a period of 25 TW/cm^2, corresponding to $\Delta U_p = \hbar\omega$ in the whole intensity regime considered. The agreement between measurements and calculations implies that the coherent capture mechanism also dominates at 800 nm.

In contrast, in the low-intensity regime (i.e., below 300 TW/cm^2) for 400 nm, though there are also clear steps in the calculated ionization and RSE curves [see Fig. 5(a)], this feature is at variance with the measurement. In the calculation results, the ionization rising trend ends at about 200 TW/cm^2, while the one for RSE just starts at this intensity and ends at around 250 TW/cm^2. On the other hand, the measured ionization and RSE probabilities increase simultaneously in this intensity regime [see Fig. 4(a)]. The discrepancy between the simulations and measurements can be more clearly found in Fig. 5(b), where the intensity dependence of the ratio of the RSE to ionization probabilities is presented. The measured and calculated curves show good agreement at high intensity but exhibits significant discrepancy at low intensity, indicating that the coherent capture picture is not important any longer in the low-intensity regime.

In fact, the experimental results in this low-intensity regime of Fig. 4(a) can be understood by considering the multiphoton resonance with ac-Stark-shifted excited states. At the intensity a little higher than the one of six-photon channel closing, dense Rydberg states (below the ionization threshold) would become resonance with the ac-Stark-shifted ground state. The efficient resonance with the Rydberg states will give rise to the sharp increase of the Ar* yield. As the atoms could be populated to the Rydberg states with a broad range of angular momenta [29,30], the Rydberg states with lower angular momenta may be able to absorb one more photon to be ionized, resulting in the singly charged Ar$^+$ via a resonant MPI process. On the other hand, the Rydberg states with higher angular momenta could survive the intense laser field and give rise to the detected neutral atoms. The large probability of six-plus-one resonant ionization process may explain the in-phase enhancement of the Ar* and Ar$^+$. It is worthwhile mentioning that, considering its quantum feature of the RSE process, both the multiphoton resonance and coherent capture mechanisms should satisfy resonance condition and are thus closely related to the channel closing effect as discussed in previous works [29,30,39,40]. The main difference lies in that the continuum states serve as the main intermediate states in the latter one but play much less or no role in the former one.

V. CONCLUSION

In summary, the intensity dependence of Ar* and Ar$^+$ yields in an intense laser field has been investigated experimentally and theoretically. At 400 nm, the measured intensity dependence of Ar* yields shows a prominent sequence of steps. The first enhancement is accompanied by the increase of Ar$^+$ yields and can be understood by multiphoton resonance mechanism, while the second enhancement appears at

the intensity where a local minimum of Ar^+ yields comes out. Moreover, at 800 nm, the yields of Ar^* exhibit significant modulations as a function of laser intensity, which are out of phase with respect to the yields of Ar^+. With the analysis by a dedicated quantum model of RSE, it is shown that the coherent recapture mechanism plays an important role in the high-intensity regime at 400 nm and also the whole intensity range explored in this work at 800 nm. Our results reveal that the mechanism of RSE experiences a transition from multiphoton resonance to coherent recapture mechanism. This finding provides a comprehensive physical picture behind the strong-field RSE process.

APPENDIX A: THE SPATIAL AND VELOCITY DISTRIBUTIONS OF THE SUPERSONIC ATOMIC BEAM

Usually, the velocity distribution of a supersonic beam can be described with the ellipsoidal drifting Maxwellian model [35,41]

$$f(v_\parallel, v_\perp) = n\left(\frac{m}{2\pi k_B T_\parallel}\right)^{\frac{1}{2}}\left(\frac{m}{2\pi k_B T_\perp}\right)$$

$$\times \exp\left[-\frac{m}{2k_B T_\parallel}(v_\parallel - \bar{v})^2 - \frac{m}{2k_B T_\perp}v_\perp^2\right], \quad (A1)$$

where m is the mass of the atom in question (Ar here), k_B the Boltzmann's constant, $T_\parallel$ and $T_\perp$ the parallel and perpendicular temperatures, $v_\parallel$ and $v_\perp$ the parallel and perpendicular components of the velocity, and $\bar{v}$ the most probable velocity of the beam along the parallel direction, where parallel (perpendicular) means the direction in question is parallel (perpendicular) to the propagation direction of the supersonic beam.

The parameters of $\bar{v} = 559$ m/s and $T_\parallel = 36.2$ K can be determined by fitting the measured time-of-flight distribution of Ar^* with the velocity distribution function $f(v_\parallel) \propto \exp[-\frac{m}{2k_B T_\parallel}(v_\parallel - \bar{v})^2]$. $T_\perp$ can be calculated by [35,42]

$$T_\perp = T_0\left(1 + \frac{\gamma - 1}{2}M^2\right)^{-1}, \quad (A2)$$

where $T_0 = 300$ K is the room temperature, γ the ratio of heat capacities, and M the Mach number, which can be

determined by [35]

$$M = A\left(\frac{y - y_0}{d}\right)^{\gamma-1} - \frac{\frac{1}{2}\left(\frac{\gamma+1}{\gamma-1}\right)}{A\left(\frac{y-y_0}{d}\right)^{\gamma-1}}, \quad \left(\frac{y}{d}\right) > 2.5 \quad (A3)$$

where A is a constant, d the nozzle diameter, y the distance between the nozzle and the skimmer along the propagation direction of the supersonic beam, and y_0 the coordinate of the virtual source (see [35,43,44] for details) from which the beam can be taken as a spherical expansion. For the supersonic beam of Ar in our experiments, these coefficients are $A = 3.26$, $\gamma = \frac{5}{3}$, $d = 50\,\mu$m, $y = 1.5$ cm, and $y_0 = 3.75\,\mu$m [35]. The off-axis density correlation for axisymmetric flow is

$$\frac{\rho(x, y, z)}{\rho(0, y, 0)} = \cos^2\theta\cos^2\left(\frac{\pi\theta}{2\phi}\right), \quad (A4)$$

where $\tan\theta = \sqrt{x^2 + z^2}/y$, $\phi = 1.365$ (a constant given in [35]), and θ the off-axis angle. The radial distance from the centerline of the supersonic beam can be calculated by $r_{xz} = \sqrt{x^2 + z^2}$. With all the parameters given above, $T_\perp = 0.04$ K can be determined. Therefore, the spatial distribution of the atomic beam at the laser focus ($y = 0.805$ m) can be described by

$$D(x, z) = \sum \frac{\rho(x, y, z)}{\rho(0, y, 0)}f(v_\parallel, v_\perp)$$

$$= \sum \cos^2\theta\cos^2\left(\frac{\pi\theta}{2\phi}\right)f(v_\parallel, v_\perp). \quad (A5)$$

Based on the above calculations, we can obtain the spatial distribution of the atomic beam. With a collimation aperture with a radius of 250 μm, the radius of transverse spatial distribution of the supersonic beam at the laser focus, which locates 0.17 m away from the aperture, has been determined to be 300 μm. The determined radius is significantly smaller than the Rayleigh length.

APPENDIX B: SIMULATION WITH FOCAL-VOLUME AVERAGING EFFECT CONSIDERED

To compare with the experimental data, focal-volume averaging has been applied to the numerical calculations. Let $d^3N/d^3\mathbf{r} \equiv P(I)$ denotes the number of electrons generated from unit volume at the intensity of I. Generally, the three-dimensional spatial intensity distributions can be given by

$$I(r, z) = I_0\left(\frac{w_0}{w(z)}\right)^2\exp\left[-2\left(\frac{r}{w(z)}\right)^n\right], \quad (B1)$$

where the order n determines the uniformity of the spatial distribution of laser intensity at the focal point (i.e., $n < 2$ for sub-Gaussian function, $n = 2$ for the Gaussian function, and $n > 2$ for the super-Gaussian function), $r = \sqrt{x^2 + y^2}$ the radial distance to the laser beam axis, z the coordinate along the laser propagation direction, and

$$w(z) = w_0[1 + (z/z_R)^2]^{\frac{1}{2}}, \quad (B2)$$

w_0 the beam waist radius at the focus, $z_R = \pi w_0^2/\lambda$ the Rayleigh length, and λ the wavelength of the radiation. The radius $r(I, z)$ of an isointensity shell of intensity I is then

given by

$$r(I, z) = w_0 \sqrt{1 + \frac{z^2}{z_R^2}} \left\{ \frac{1}{2} \left[\ln\left(\frac{I_0}{I}\right) - \ln\left(1 + \frac{z^2}{z_R^2}\right) \right] \right\}^{\frac{1}{n}}.$$

(B3)

In some cases, the geometry of the interaction volume is closer to one-dimensional or two-dimensional case. In the one-dimensional focal-volume averaging, let $dN/dr = P(I)$ and the yields achieved within the focal volume are

$$N_{1D} = \int P(I) \frac{dr}{dI} dI$$

$$= \frac{w_0}{n \times 2^{\frac{1}{n}}} \int_0^{I_0} \frac{dI}{I} \left[\ln\left(\frac{I_0}{I}\right) \right]^{\frac{1-n}{n}} P(I).$$

(B4)

In the two-dimensional case, let $d^2N/d^2\mathbf{r} \equiv P(I)$ and the spatial intensity distribution can be given by

$$I(r) = I_0 \exp\left[-2\left(\frac{r}{w_0}\right)^n \right].$$

(B5)

The two-dimensional area S is

$$S = \pi r^2 = \pi w_0^2 \left[\frac{1}{2} \ln\left(\frac{I_0}{I}\right) \right]^{\frac{2}{n}}.$$

(B6)

The yields achieved within the focal volume are

$$N_{2D} = \int P(I) \frac{dS}{dI} dI$$

$$= \frac{\pi w_0^2}{n \times 2^{\frac{2-n}{n}}} \int_0^{I_0} \left[\ln\left(\frac{I_0}{I}\right) \right]^{\frac{2-n}{n}} \frac{dI}{I} P(I).$$

(B7)

For the three-dimensional case, the isointensity shell volume can be analytically integrated for the Gaussian beam ($n = 2$), which is given by

$$V_{full} = \pi \int_{-z_{max}}^{z_{max}} r^2(I, z) dz = \pi w_0^2 z_R$$

$$\times \left[\frac{4}{3} \sqrt{\frac{I_0}{I} - 1} + \frac{2}{9} \left(\frac{I_0}{I} - 1\right)^{\frac{3}{2}} \right.$$

$$\left. - \frac{4}{3} \arctan\left(\sqrt{\frac{I_0}{I} - 1} \right) \right],$$

(B8)

where z_{max} can be calculated by

$$z_{max}(I) = z_R \sqrt{\frac{I_0}{I} - 1}.$$

(B9)

The yields achieved within the isointensity shell volume are

$$N_{3D} = \int P(I) \frac{dV_{full}}{dI} dI$$

$$= \frac{\pi w_0^2 z_R}{3} \int_0^{I_0} \frac{dI}{I^{\frac{5}{2}}} \sqrt{I_0 - I}(2I + I_0) P(I).$$

(B10)

In fact, as shown in Fig. 2, at the laser focus, the measured spatial distribution of laser intensity can be well fitted by a SG function [Eq. (B5)] with $n = 2.45$. Thus, the spatial intensity distributions for the SG beam applied in our experiments can be given by Eq. (B1). In this case, the yields achieved with
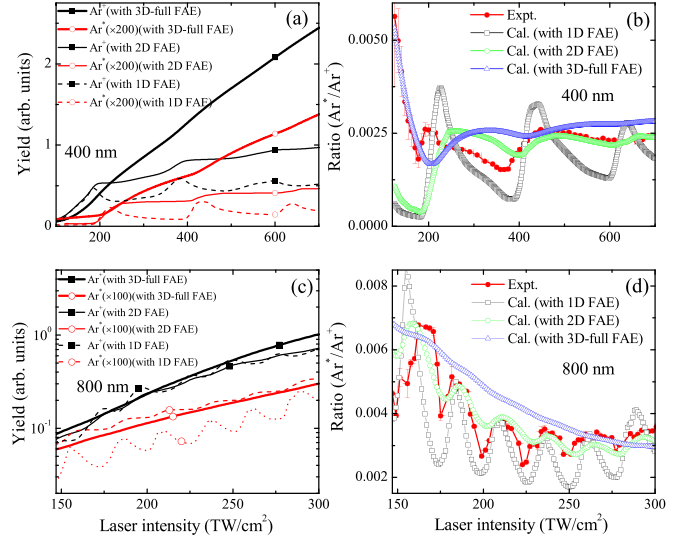

FIG. 6. (a), (c) The calculated intensity dependence of ionization and excitation yields for Ar subject to the 400-nm (a) and 800-nm (c) laser fields. Black lines: ionization yields calculated with 1D (thin dashed lines), 2D (thin solid lines), and 3D (thick solid lines) focal averaging effect (FAE) included. Red lines: RSE yields calculated with 1D (thin dashed lines), 2D (thin solid lines), and 3D (thick solid lines) FAE included. (b), (d) The measured and calculated intensity dependence of the ratio of excitation yields to ionization yields for Ar subject to a 400-nm (b) and 800-nm (d) laser fields. Solid red circles: the measured intensity dependence of the ratio of excitation yields to ionization yields. Open black square: the ratio calculated with 1D FAE included. Open green circle: the ratio calculated with 2D FAE included. Open blue triangle: the ratio calculated with 3D FAE included. Note that the influence of FAE is included in Eq. (B4) for the 1D, Eq. (B7) for the 2D, and Eq. (B10) for the 3D cases. The calculated excitation yield is a sum of the contributions of Rydberg states from $n = 5$ to 16 and has been multiplied by 200 or 100 for better visualization.

focal averaging effect included are given by

$$N_{expt} = \int D(x, z) P(I(r, z)) dV.$$

(B11)

To demonstrate the significance of the focal averaging effect, using Eqs. (B4), (B7), and (B10), we have performed the calculations for the one-dimensional, two-dimensional, and three-dimensional focal-volume averaging cases for Gaussian beam and the results are shown in Fig. 6. Apparently, the oscillations are mostly prominent in the one-dimensional case and still obvious in the two-dimensional case, while the oscillations become less obvious in the three-dimensional case.

To compare the impact of the different target geometry in the case of the SG beam and that of a Gaussian beam, the numerical simulations of peak intensity dependence of the isointensity volume of a chosen intensity range have been performed and the results are shown in Fig. 7(a). Three cases have been considered, i.e., one-dimensional, two-dimensional, and three-dimensional cases. As shown in Fig. 7(a), the calculated volume is smaller for SG beam in all three cases. Especially, for the Gaussian beam, the calculated isointensity volume in two-dimensional case is a constant with respect to the peak intensity. On the contrary, for the SG beam, the isointensity volume in two-dimensional case decreases with increasing
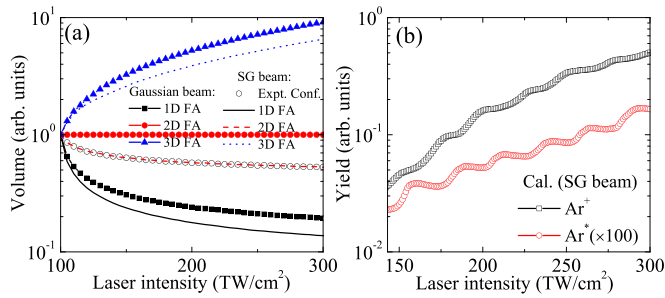
FIG. 7. (a) Calculated peak intensity dependence of the isointensity volume of the intensity range of [90, 100 TW/cm^2]. The black open circle represents the result calculated with the parameters chosen according to the experimental configurations, where the spatial distribution of the intensity of the SG beam has been employed in the focus. The curves with (without) symbols represent calculation results for the Gaussian (SG) beam. The black (lower two), red (middle two), and blue (upper two) curves represent the results for the one-dimensional, two-dimensional, and three-dimensional target geometries, respectively. (b) Calculated intensity dependence of Ar$^+$ (black squares) and Ar* (red circles) yields with SG laser intensity distributions at 800 nm. The latter has been multiplied by 100 for a better visualization.

peak intensity. If the parameters of the target geometry have been set according to the experimental configurations, the calculated peak intensity dependence of the isointensity volume almost matches that of the two-dimensional case for SG beam. This result can be attributed to the fact that the width of the transverse spatial distribution of gas beam at focus is much smaller than the Rayleigh length (see Fig. 3 and the discussions on supersonic beam above). The results, which have been calculated with Eq. (B11) and the parameters chosen according to the experimental configurations, are shown in Figs. 5 and 7(b). The calculations can qualitatively reproduce the main features of the measurements. It is worthwhile mentioning that there are still some quantitative discrepancies between the theoretical and experimental results. For example, the dips are more pronounced in the experimental yields than that in the calculation. One possible reason for these disagreements is that the spatial resolution of available commercial digital camera is not good enough to resolve the subtle spatial distribution of the focus (comparing resolution of 5.5 μm to the FWHM of the laser focus of about 30 to 40 μm shown in Fig. 2), which could be in fact more flat than the fitted SG distribution near the center of the beam, leading to faster decreasing isointensity volume than that shown in Fig. 7(a) when the peak intensity increases.

[1] P. Agostini, F. Fabre, G. Mainfray, G. Petite, and N. K. Rahman, Free-Free Transitions Following Six-Photon Ionization of Xenon Atoms, Phys. Rev. Lett. **42**, 1127 (1979).

[2] L. F. DiMauro and P. Agostini, Ionization dynamics in strong laser fields, Adv. At. Mol. Opt. Phys. **35**, 79 (1995).

[3] W. Becker, F. Grasbon, R. Kopold, D. B. Milošević, G. G. Paulus, and H. Walther, Above-threshold ionization: From classical features to quantum effects, Adv. At. Mol. Opt. Phys. **48**, 35 (2002).

[4] D. B. Milošević and F. Ehlotzky, Scattering and reaction processes in powerful laser fields, Adv. At. Mol. Opt. Phys. **49**, 373 (2003).

[5] P. Agostini and L. F. DiMauro, Atoms in high intensity mid-infrared pulses, Contemp. Phys. **49**, 179 (2008).

[6] L. V. Keldysh, Ionization in the field of a strong electromagnetic wave, ZhETF **47**, 1945 (1965) [Sov. Phys.–JETP **20**, 1307 (1965)].

[7] B. Walker, E. Mevel, B. Yang, P. Breger, J. P. Chambaret, A. Antonetti, L. F. DiMauro, and P. Agostini, Double ionization in the perturbative and tunneling regimes, Phys. Rev. A **48**, R894 (1993).

[8] E. Mevel, P. Breger, R. Trainham, G. Petite, P. Agostini, A. Migus, J. P. Chambaret, and A. Antonetti, Atoms in Strong Optical Fields: Evolution from Multiphoton to Tunnel Ionization, Phys. Rev. Lett. **70**, 406 (1993).

[9] J. L. Chaloupka, J. Rudati, R. Lafon, P. Agostini, K. C. Kulander, and L. F. DiMauro, Observation of a Transition in the Dynamics of Strong-Field Double Ionization, Phys. Rev. Lett. **90**, 033002 (2003).

[10] J. Rudati, J. L. Chaloupka, P. Agostini, K. C. Kulander, and L. F. DiMauro, Multiphoton Double Ionization via Field-Independent Resonant Excitation, Phys. Rev. Lett. **92**, 203001 (2004).

[11] P. Hansch, M. A. Walker, and L. D. Van Woerkom, Eight- and nine-photon resonances in multiphoton ionization of xenon, Phys. Rev. A **57**, R709 (1998).

[12] G. G. Paulus, W. Nicklich, Huale Xu, P. Lambropoulos, and H. Walther, Plateau in Above Threshold Ionization Spectra, Phys. Rev. Lett. **72**, 2851 (1994).

[13] C. Y. Wu, Y. D. Yang, Y. Q. Liu, Q. H. Gong, M. Y. Wu, X. Liu, X. L. Hao, W. D. Li, X. T. He, and J. Chen, Characteristic Spectrum of Very Low-Energy Photoelectron from Above-Threshold Ionization in the Tunneling Regime, Phys. Rev. Lett. **109**, 043001 (2012).

[14] L. Guo, S. S. Han, X. Liu, Y. Cheng, Z. Z. Xu, J. Fan, J. Chen, S. G. Chen, W. Becker, C. I. Blaga, A. D. DiChiara, E. Sistrunk, P. Agostini, and L. F. DiMauro, Scaling of the Low-Energy Structure in Above-Threshold Ionization in the Tunneling Regime: Theory and Experiment, Phys. Rev. Lett. **110**, 013001 (2013).

[15] M. P. de Boer and H. G. Muller, Observation of Large Populations in Excited States After Short-Pulse Multiphoton Ionization, Phys. Rev. Lett. **68**, 2747 (1992).

[16] R. R. Jones, D. W. Schumacher, and P. H. Bucksbaum, Population trapping in Kr and Xe in intense laser fields, Phys. Rev. A **47**, R49 (1993).

[17] A. Talebpour, C.-Y. Chien, and S. L. Chin, Population trapping in rare gases, J. Phys. B: At., Mol. Opt. Phys. **29**, 5725 (1996).

[18] A. Talebpour, Y. Liang, and S. L. Chin, Population trapping in the CO molecule, J. Phys. B: At. Mol. Opt. Phys. **29**, 3435 (1996).

[19] A. Azarm, S. M. Sharifi, A. Sridharan, S. Hosseini, Q. Q. Wang, A. M. Popov, O. V. Tikhonova, E. A. Volkova, and S. L. Chin, Population trapping in Xe atoms, J. Phys.: Conf. Ser. **414**, 012015 (2013).

[20] M. V. Fedorov, N. P. Polucktov, A. M. Popov, O. V. Tikhonova, V. Yu. Kharin, and E. A. Volkova, Interference stabilization revisited, IEEE J. Sel. Top. Quantum Electron. **18**, 42 (2012).

[21] A. M. Popov, O. V. Tikhonova, and E. A. Volkova, Population trapping of excited atoms in strong chirped laser pulses, J. Phys. B: At., Mol. Opt. Phys. **47**, 204012 (2014).

[22] T. Nubbemeyer, K. Gorling, A. Saenz, U. Eichmann, and W. Sandner, Strong-Field Tunneling without Ionization, Phys. Rev. Lett. **101**, 233001 (2008).

[23] B. B. Wang, X. F. Li, P. M. Fu, J. Chen, and J. Liu, Coulomb potential recapture effect in above-barrier ionization in laser pulses, Chin. Phys. Lett. **23**, 2729 (2006).

[24] U. Eichmann, T. Nubbemeyer, H. Rottke, and W. Sandner, Acceleration of neutral atoms in strong short-pulse laser fields, Nature (London) **461**, 1261 (2009).

[25] U. Eichmann, A. Saenz, S. Eilzer, T. Nubbemeyer, and W. Sandner, Observing Rydberg Atoms to Survive Intense Laser Fields, Phys. Rev. Lett. **110**, 203002 (2013).

[26] H. Zimmermann, J. Buller, S. Eilzer, and U. Eichmann, Strong-Field Excitation of Helium: Bound State Distribution and Spin Effects, Phys. Rev. Lett. **114**, 123003 (2015).

[27] S. Larimian, S. Erattupuzha, C. Lemell, S. Yoshida, S. Nagele, R. Maurer, A. Baltuška, J. Burgdörfer, M. Kitzler, and X. H. Xie, Coincidence spectroscopy of high-lying Rydberg states produced in strong laser fields, Phys. Rev. A **94**, 033401 (2016).

[28] H. Yun, J. H. Mun, S. I. Hwang, S. B. Park, I. A. Ivanov, C. H. Nam, and K. T. Kim, Coherent extreme-ultraviolet emission generated through frustrated tunneling ionization, Nat. Photonics **12**, 620 (2018).

[29] Q. Li, X. M. Tong, T. Morishita, H. Wei, and C. D. Lin, Fine structures in the intensity dependence of excitation and ionization probabilities of hydrogen atoms in intense 800-nm laser pulses, Phys. Rev. A **89**, 023421 (2014).

[30] B. Piraux, F. Mota-Furtado, P. F. O'Mahony, A. Galstyan, and Yu. V. Popov, Excitation of Rydberg wave packets in the tunneling regime, Phys. Rev. A **96**, 043403 (2017).

[31] A. T. J. B. Eppink and D. H. Parker, Velocity map imaging of ions and electrons using electrostatic lenses: Application in photoelectron and photofragment ion imaging of molecular oxygen, Rev. Sci. Instrum. **68**, 3477 (1997).

[32] K. Thyagarajan and A. Ghatak, in *Lasers: Fundamentals and Applications*, edited by R. Needs, W. T. Rhodes, H. E. Stanley (Springer, New York, 2011).

[33] M. Mishra, and W. P. Hong, Investigation on propagation characteristics of super-Gaussian beam in highly nonlocal medium, Prog. Electromagn. Res. B **31**, 175 (2011).

[34] X. H. Wang, Z. Y. Xu, and Q. Wang, Propagation of coupled super-Gaussian beam pairs in strong nonlocal media, Optik **126**, 4977 (2015).

[35] D. R. Miller, in *Atomic and Molecular Beam Methods*, edited by G. Scoles, D. Bassi, U. Buck, and D. Laine (Oxford University Press, New York, 1988), Vol. 1, p. 14.

[36] A. M. Perelomov, V. S. Popov, and M. V. Terent'ev, Ionization of atoms in an alternating electric field: II, ZhETF **51**, 309 (1967) [Sov. Phys.–JETP **24**, 207 (1967)].

[37] F. H. M. Faisal, Multiple absorption of laser photons by atoms, J. Phys. B: At., Mol. Phys. **6**, L89 (1973); H. R. Reiss, Effect of an intense electromagnetic field on a weakly bound system, Phys. Rev. A **22**, 1786 (1980).

[38] S. L. Hu, X. L. Hao, H. Lv, M. Q. Liu, T. X. Yang, H. F. Xu, M. X. Jin, D. J. Ding, Q. G. Li, W. D. Li, W. Becker, and J. Chen, Quantum dynamics of atomic Rydberg excitation in an intense laser field, Opt. Express **27**, 31629 (2019).

[39] H. Zimmermann, S. Patchkovskii, M. Ivanov, and U. Eichmann, Unified Time and Frequency Picture of Ultrafast Atomic Excitation in Strong Laser Fields, Phys. Rev. Lett. **118**, 013003 (2017).

[40] D. Chetty, R. D. Glover, B. A. deHarak, X. M. Tong, H. Xu, T. Pauly, N. Smith, K. R. Hamilton, K. Bartschat, J. P. Ziegel, N. Douguet, A. N. Luiten, P. S. Light, I. V. Litvinyuk, and R. T. Sang, Observation of dynamic Stark resonances in strong-field excitation, Phys. Rev. A **101**, 053402 (2020).

[41] L. Pedemonte, G. Bracco, and R. Tatarek, Theoretical and experimental study of He free-jet expansions, Phys. Rev. A **59**, 3084 (1999).

[42] G. M. McClelland, K. L. Saenger, J. J. Valentini, and D. R. Herschbach, Vibrational and rotational relaxation of iodine in seeded supersonic beams, J. Phys. Chem. **83**, 947 (1979).

[43] S. D. Eder, G. Bracco, T. Kaltenbacher, and B. Holst, Two Dimensional Imaging of the Virtual Source of a Supersonic Beam: Helium at 125 K, J. Phys. Chem. A **118**, 4 (2014).

[44] H. C. W. Beijerinck and N. F. Verster, Absolute intensities and perpendicular temperatures of supersonic beams of polyatomic gases, Phys. B+C (Amsterdam) **111**, 327 (1981).